AIP | Applied Physics Letters

Superconductivity induced by Se-doping in layered charge-density-wave system 1T-TaS2−xSex

Y. Liu, R. Ang, W. J. Lu, W. H. Song, L. J. Li et al.

Citation: Appl. Phys. Lett. **102**, 192602 (2013); doi: 10.1063/1.4805003
View online: http://dx.doi.org/10.1063/1.4805003
View Table of Contents: http://apl.aip.org/resource/1/APPLAB/v102/i19
Published by the AIP Publishing LLC.

Superconductivity induced by Se-doping in layered charge-density-wave system 1*T*-$TaS_{2-x}Se_x$

Y. Liu,[1] R. Ang,[1,2,a)] W. J. Lu,[1] W. H. Song,[1] L. J. Li,[1] and Y. P. Sun[1,3,a)]
[1]*Key Laboratory of Materials Physics, Institute of Solid State Physics, Chinese Academy of Sciences, Hefei 230031, People's Republic of China*
[2]*WPI Research Center, Advanced Institute for Materials Research, Tohoku University, Sendai 980-8577, Japan*
[3]*High Magnetic Field Laboratory, Chinese Academy of Sciences, Hefei 230031, People's Republic of China*

(Received 12 April 2013; accepted 29 April 2013; published online 14 May 2013)

Layered 1*T*-$TaS_{2-x}Se_x$ ($0 \leq x \leq 2$) single crystals have been systematically fabricated by a chemical vapor transport technique. Surprisingly, the superconductivity is induced by the Se doping. We demonstrate the appearance of a series of electronic states: the Mott phase melts into a nearly commensurate charge-density-wave (CDW) phase, superconductivity in a wide x range develops within the nearly commensurate CDW state, and finally commensurate CDW phase reproduces for heavy Se content. The rich phase diagram provides an ideal platform to investigate the interplay between electron correlation, CDW, and superconductivity, as well as the potential applications in electronic devices. © *2013 AIP Publishing LLC*. [http://dx.doi.org/10.1063/1.4805003]

In the past few years, especially after the synthesis of monolayer MoS_2, transition-metal dichalcogenides (TMDs) have triggered a tremendous wave of excitement in the scientific community due to their unique structural properties and semiconducting nature.[1–8] On the other hand, it is worth noting that layered TMDs also provide an excellent platform to investigate the interplay between electron correlation, charge-density-wave (CDW), superconductivity, and other electronic orders, essentially taking into account its quasi-two-dimensional crystal structure susceptible to various electronic instabilities.[9,10] As is well known, CDW and superconductivity are two of the most fundamental collective quantum phenomena in low-dimensional electron systems. The CDW is periodic modulation of the density of conduction electrons in solids. The CDW often appears in the proximity of superconductivity near the Mott insulating phase, while the CDW is generally believed to be competing with superconductivity.[11–14]

Amongst many TMDs, 1*T*-TaS_2 and 1*T*-$TaSe_2$ have attracted special attention due to their unique characteristics related to the formation of CDW.[15] Both materials have the same CdI_2-type structure with the space group $P\text{-}3m1$, composed of planes of hexagonally arranged Ta atoms, sandwiched by two chalcogen (S and Se) layers coordinating the central Ta atom in an octahedral arrangement as shown in Figs. 1(a) and 1(c). Although these two materials have very similar crystal structure and CDW superstructure, they exhibit dramatically different electrical properties. In particular, 1*T*-TaS_2 is characterized by a high-temperature normal metallic phase, followed by a nearly commensurate CDW (NCCDW) phase and commensurate CDW (CCDW) phase coexisting with a Mott insulating phase. In comparison, 1*T*-$TaSe_2$ undergoes a high-temperature normal metal to CCDW transition without drastic change in the electronic conductivity in the whole CCDW phase, and presents a metallic behavior.

The Mott insulating phase of 1*T*-TaS_2 is unusual, Ta atoms are displaced to form David-star clusters where twelve Ta atoms contract toward central atom, and each cluster is interlocked by forming triangular superlattice with a $\sqrt{13} \times \sqrt{13}$ periodicity,[15–19] accompanied by the narrowing of the Ta 5*d* valence band and the formation of multiple subbands due to band folding.[20,21] With increasing the temperature, the Mott phase of 1*T*-TaS_2 melts into the NCCDW phase with a sudden resistivity drop, where several tens of stars organize into roughly hexagonal domains.[22] On the other hand, a strong CCDW phase of 1*T*-$TaSe_2$ arises until high temperature, holding a $\sqrt{13}\times\sqrt{13}$ superstructure,[15,23–25] analogous to the low-temperature CCDW phase of 1*T*-TaS_2.

Until now, superconductivity emerges in 1*T*-TaS_2 by applying high pressure[26] or introducing disorders in the crystal.[27] It has been recently reported that the substitution of Ta with light Fe content in 1*T*-$Fe_xTa_{1-x}S_2$ ($0 \leq x \leq 0.05$) induces superconductivity in the NCCDW state on the verge of Mott and Anderson localization.[28] More importantly, the high-resolution angle-resolved photoemission spectroscopy (ARPES)[29] directly accessed the essential issue to elucidate the electronic states of all the available electronic phases in 1*T*-$Fe_xTa_{1-x}S_2$, where the superconductivity is characterized by a shallow electron pocket at the Brillouin-zone center, the superconductivity, and the NCCDW state coexist in the real space. Even so, an investigation on the emergence of superconductivity by the substitution of S site has not yet been made. We wondered the superconductivity in 1*T*-TaS_2 whether it is the intrinsic universality and not dependent on the substitution of Ta site or S site.

In this letter, high-quality single crystals of 1*T*-$TaS_{2-x}Se_x$ ($0 \leq x \leq 2$) were grown by the chemical vapor transport (CVT) method with iodine as a transport agent. The crystal structure was identified by x-ray diffraction (XRD). The XRD patterns were obtained on a Philips X'pert PRO diffractometer with Cu k_α radiation at room

a)Authors to whom correspondence should be addressed. Electronic addresses: rang@issp.ac.cn and ypsun@issp.ac.cn

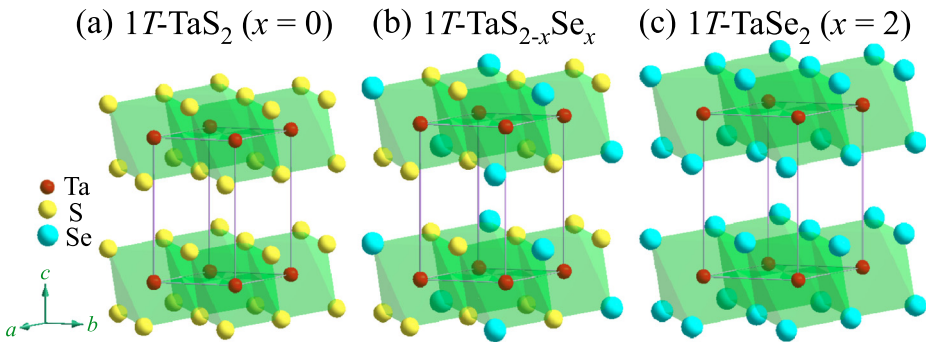

FIG. 1. Crystal structure of (a) pristine 1*T*-TaS_2 ($x=0$), (b) 1*T*-$TaS_{2-x}Se_x$, and (c) pristine 1*T*-$TaSe_2$ ($x=2$).

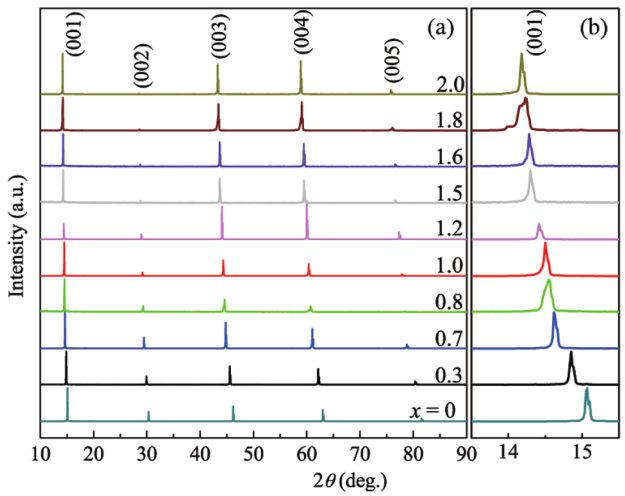

FIG. 2. (a) Single-crystal XRD patterns of 1*T*-$TaS_{2-x}Se_x$. (b) The evolution of diffraction peak along the (001) direction for all of samples.

temperature. Structural refinements were performed by using Rietveld method with the X'Pert High Score Plus software. The average stoichiometry was determined by examination of multiple points using x-ray energy dispersive spectroscopy (EDS) with a scanning electron microscopy (SEM). The EDS results indicate that the actual concentration x is close to the nominal one. The resistivity measurements (ρ) down to 2.0 K were carried out by the standard four-probe method in a Quantum Design Physical Property Measurement System (PPMS). The magnetic susceptibility (χ) was measured in both zero-field-cooled (ZFC) and field-cooled (FC) modes down to 2.0 K using a Quantum Design superconducting quantum interference device (SQUID) system.

The crystal structure of 1*T*-$TaS_{2-x}Se_x$ resembles the pristine 1*T*-TaS_2 and 1*T*-$TaSe_2$ [see Fig. 1(b)]. As shown in Fig. 2(a), only (00l) reflections were observed in the single-crystal XRD patterns for each sample, indicating that the crystallographic c axis is perpendicular to the plane of the single crystal. With increasing the Se content, the diffraction peak along the (00l) direction distinctly shifts to lower angle [see Fig. 2(b)], confirming the larger lattice parameter of Se than that of S.

Structural refinement of powder XRD identifies that all reflections can be indexed in the *P*-3*m*1 space group. Figures 3(a)–3(c) show the XRD patterns and the structural refinement results of Rietveld analysis for the selected samples with $x=2$, 1, and 0. For the Rietveld fitting, Ta and S (Se) atoms are placed at the 1*a* (0, 0, 0) and 2*d* (1/3, 2/3, 1/4) positions, respectively. The refined structural parameters and selected bond lengths and angles are listed in Table I. For $x=0$, the lattice parameters are $a=3.3672(6)$ Å and $c=5.9020(9)$ Å. For $x=1$, the lattice parameters are $a=3.4173(8)$ Å and $c=6.1466(4)$ Å. For $x=2$, the lattice parameters are $a=3.4746(9)$ Å and $c=6.2778(4)$ Å. Comparatively, the lattice distortion along c axis is stronger than that of ab plane from $x=0$ to $x=2$. In Table I, it can reflect the information

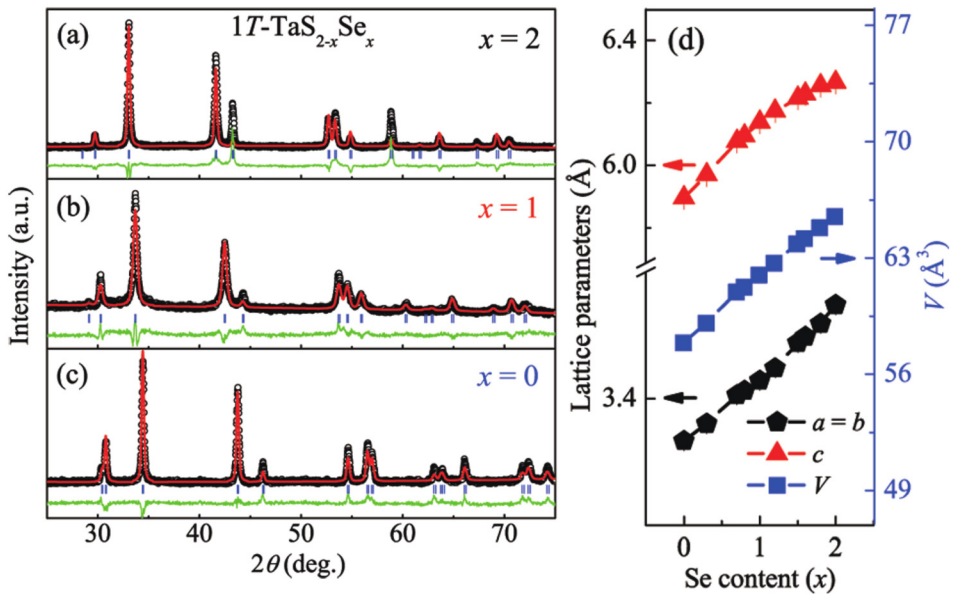

FIG. 3. Structural characterization of 1*T*-$TaS_{2-x}Se_x$. (a)-(c) Powder XRD patterns with Rietveld refinement for the selected samples with $x=2$, 1, and 0, respectively. (d) The lattice parameters a, c, and unit cell volume (V) as a function of x.

TABLE I. Structural parameters and selected bond lengths and angles of 1*T*-$TaS_{2-x}Se_x$ ($x = 0$, 1, and 2) from powder XRD Rietveld refinement.

Formula	1*T*-TaS_2 ($x = 0$)	1*T*-TaSSe ($x = 1$)	1*T*-$TaSe_2$ ($x = 2$)
Space group	*P*-3*m*1	*P*-3*m*1	*P*-3*m*1
Z	1	1	1
a (Å)	3.3672(6)	3.4173(8)	3.4746(9)
c (Å)	5.9020(9)	6.1466(4)	6.2778(4)
$d_{Ta-S(Se)}$ (Å)	2.441	2.501	2.547
$\theta_{S(Se)-Ta-S(Se)}$ (°)	87.234	86.196	86.014
Cell volume (Å^3)	57.955(5)	62.166(2)	65.641(5)
Density (g cm^{-3})	7.02	7.80	8.57
R_p (%)	15.03	5.15	8.91
R_{wp} (%)	17.47	6.39	14.08
χ^2	2.00	3.79	14.97

of lattice distortion by the decrease of bond angles (θ) from θ_{S-Ta-S} (87.234°) to $\theta_{Se-Ta-Se}$ (86.014°). Figure 3(d) shows the variation of lattice parameters (*a*, *c*) and unit cell volume (*V*) with Se content. The values of *a*, *c*, and *V* monotonously increase with Se content, in accordance with the larger ion radius of Se than that of S. This is totally different from the case of the substitution of Fe at Ta site in 1*T*-$Fe_xTa_{1-x}S_2$,[28] where the values of *c* almost have no change with increasing Fe content, while the values of *a* decrease due to the smaller ion radius of Fe than that of Ta.

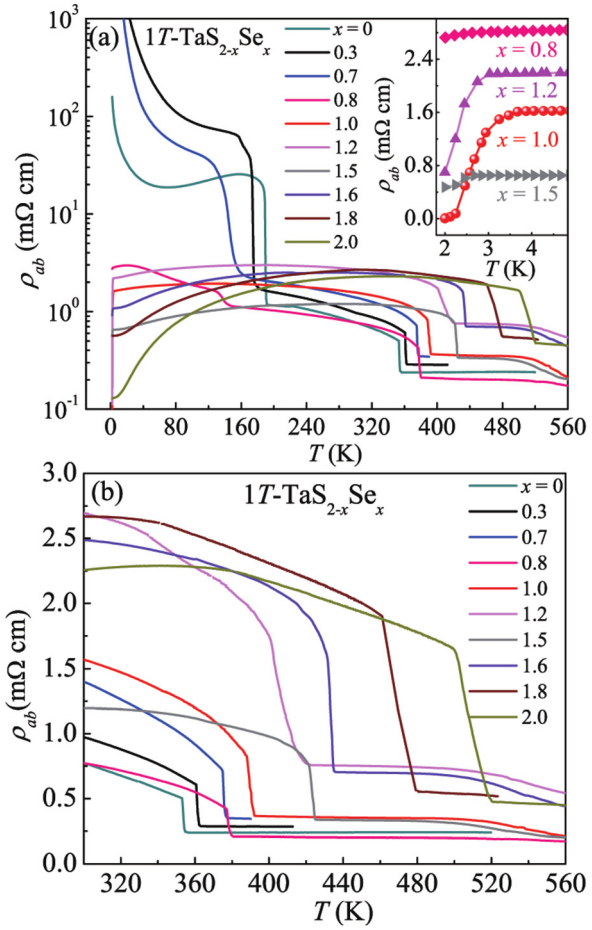

FIG. 4. (a) Temperature dependence of in-plane resistivity (ρ_{ab}) of 1*T*-$TaS_{2-x}Se_x$. The inset magnifies the region of the superconducting transitions. (b) The NCCDW transitions at high temperatures of all the samples.

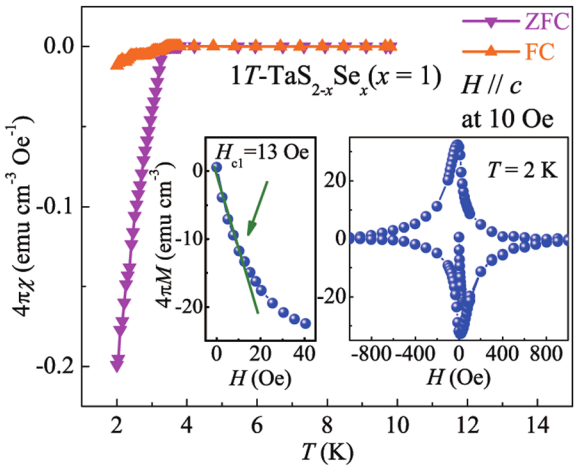

FIG. 5. Temperature dependence of magnetic susceptibility for optimally superconducting sample 1*T*-TaSSe ($x = 1$). The left inset shows the initial *M*(*H*) isotherm at 2 K, where the light green line stands for the linear fitting in the low-field range. The right inset shows the magnetization hysteresis loops of 1*T*-TaSSe at 2 K with *H* parallel to the *c*-axis.

The temperature dependence of in-plane resistivity (ρ_{ab}) measurements on 1*T*-$TaS_{2-x}Se_x$ ($0 \le x \le 2$) is shown in Fig. 4(a). At first below 200 K, it is observed a first-order transition from the NCCDW to the CCDW phase. The CCDW transition gradually shifts to lower temperature with increasing *x* content, and the Mott insulating phase at low temperatures completely disappears for $x > 0.8$. More significantly, the signature of superconductivity emerges for $x = 0.9$. The maximum of superconducting onset temperature is ~3.6 K for the optimal sample with $x = 1$ [see the inset of Fig. 4(a)]. Above $x > 1.6$, the superconductivity at low temperatures is suppressed, while CCDW phase reproduces and a metallic behavior arises until $x = 2$. Figure 4(b) shows the high-temperature resistivity to magnify the NCCDW transition from normal metallic phase. The NCCDW transition obviously shifts to higher temperature with Se content, in agreement with the larger ion radius of Se than that of S.

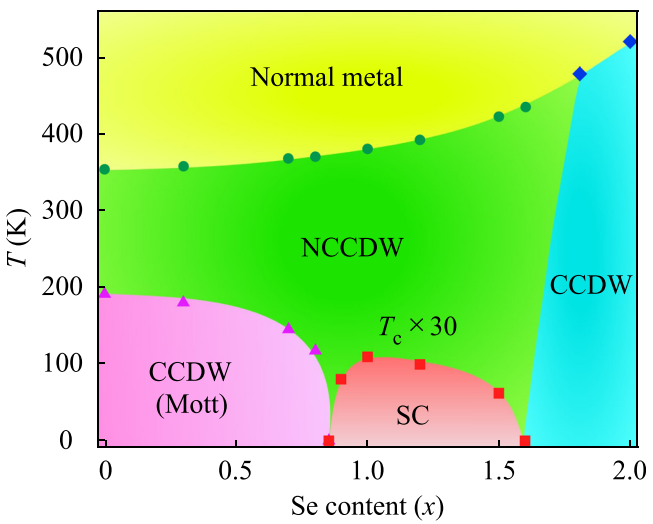

FIG. 6. Electronic phase diagram of 1*T*-$TaS_{2-x}Se_x$ derived from the present transport properties as a function of temperature and *x*, where CCDW, NCCDW, and SC represent the commensurate CDW, nearly commensurate CDW, and superconductivity, respectively.

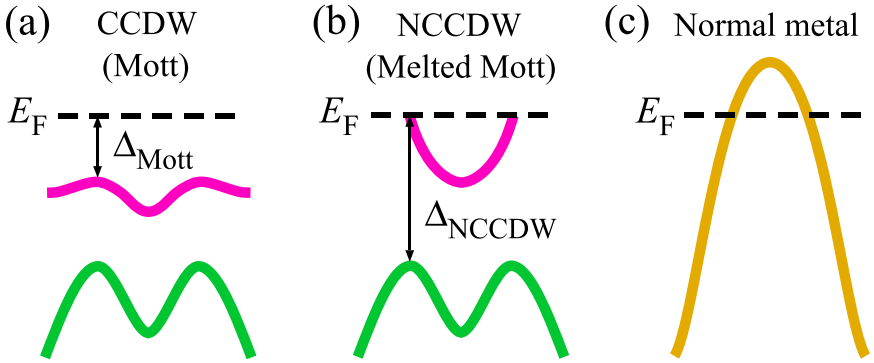

FIG. 7. Schematic band diagram of 1*T*-$TaS_{2-x}Se_x$ in (a) CCDW (Mott) phase, (b) NCCDW (melted Mott) phase, and (c) normal metallic phase, respectively. The Δ_{Mott} and Δ_{NCCDW} denotes the Mott gap and NCCDW gap, respectively.

Figure 5 shows the magnetic properties of optimally superconducting sample for 1*T*-TaSSe ($x = 1$) at 10 Oe with magnetic field H parallel to the c-axis. Undoubtedly, the diamagnetism signals at low temperatures demonstrate the occurrence of superconductivity, corresponding with the resistivity data. The steep transition reveals that the sample is rather homogeneous. The superconducting transition temperature T_c defined by the onset point of ZFC and FC curves is ~3.5 K for 1*T*-TaSSe ($x = 1$), which is higher than that of T_c (~2.1 K) for the optimally superconducting $1T - Fe_{0.02}Ta_{0.98}S_2$.[28] The left inset of Fig. 5 shows the initial $M(H)$ curve of $x = 1$ in the low-field region at 2 K. We can get the value of lower critical field ($H_{c1} \sim 13$ Oe), marked by an arrow from the point where this curve deviates from linearity. The obtained slope of the linear fitting up to 13 Oe for present experimental data is −0.955, which is accordant with $-4\pi M = H$, describing the Meissner shielding effect. The right inset of Fig. 5 shows the magnetization hysteresis loop for $x = 1$ at 2 K. The shape of $M(H)$ curve further demonstrates that the present 1*T*-TaSSe sample is a typical type-II superconductor.

Figure 6 summarizes the overall electronic phase diagram as a function of temperature and x in 1*T*-$TaS_{2-x}Se_x$. The Mott localization and the CCDW phase are evidently suppressed for $x > 0.8$. After that, a superconducting state emerges in a wide range until for $x = 1.6$. The x dependence of superconducting transition temperature T_c follows a dome-like shape. Ultimately, the superconductivity disappears and CCDW phase is induced again. In fact, the T_c-dome shape is also observed in the superconducting 1*T*-$Fe_xTa_{1-x}S_2$ by the substitution of Ta site, although it only occurs in a very narrow x range from $x = 0.01$ to 0.04.[28] It is demonstrated that the extra carriers induced by Fe substitution are not responsible to the emergence of superconductivity. In particular, no any experimental evidence on Fe 3*d* band is observed near the Fermi level, and only Ta 5*d* band contributes to the superconductivity.[29] In other words, the superconductivity is not dependent on the substitution of S or Ta site. We will discuss implications of superconductivity as below.

Taking into account the universal superconducting nature for the substitution of S or Ta site in 1*T*-TaS_2 systems, the schematic band diagram of 1*T*-$TaS_{2-x}Se_x$ is shown in Fig. 7. In the normal metallic phase, it is a weakly correlated metal where the one-electron approach entirely explains the band dispersion [see Fig. 7(c)]. In the NCCDW (melted Mott) phase, a shallow electron pocket only appears and characterizes the transport properties of the NCCDW phase as well as superconductivity as shown in Fig. 7(b). The electron pocket is gapped in the Mott phase [see Fig. 7(a)] due to the enhanced electron correlation, implying the competing nature of superconductivity with Mott localization. The intrinsic superconductivity should be characterized by the electron pocket, and also reflected by robust Ta 5*d* band. The universal nature in 1*T*-TaS_2 systems further demonstrates that superconductivity and NCCDW phase coexist in the real space.

From a viewpoint of applied prospect, controlling the superconductivity and CDW phases in present functional materials could be used for electronic devices. Switching between the insulating CDW phase and the normal metallic state could enable different types of electronic devices. Especially, it is noted that scanning tunneling microscopy and atomic force microscopy have revealed that CDW phases in 1*T*-TaS_2 systems have huge potential for promising applications.[30,31]

In summary, layered 1*T*-$TaS_{2-x}Se_x$ ($0 \le x \le 2$) single crystals have been systematically prepared by using the CVT technique. Controlling the Se content in 1*T*-$TaS_{2-x}Se_x$ could modulate various phases like Mott insulating phase, NCCDW phase, superconductivity, CCDW phase, and normal metallic phase. Our results not only render to recognize the rich phase diagram but also provide a deep insight into the interplay between electron correlation, CDW, and superconductivity.

This work was supported by the National Key Basic Research under Contract No. 2011CBA00111, and the Joint Funds of the National Natural Science Foundation of China and the Chinese Academy of Sciences' Large-scale Scientific Facility (Grand No. U1232139).

[1]J. N. Coleman, M. Lotya, A. ONeill, S. D. Bergin, P. J. King, U. Khan, K. Young, A. Gaucher, S. De, R. J. Smith, I. V. Shvets, S. K. Arora, G. Stanton, H.-Y. Kim, K. Lee, G. T. Kim, G. S. Duesberg, T. Hallam, J. J. Boland, J. J. Wang, J. F. Donegan, J. C. Grunlan, G. Moriarty, A. Shmeliov, R. J. Nicholls, J. M. Perkins, E. M. Grieveson, K. Theuwissen, D. W. McComb, P. D. Nellist, and V. Nicolosi, Science **331**, 568 (2011).
[2]C. Ataca, H. Sahin, E. Akturk, and S. Ciraci, J. Phys. Chem. C **115**, 3934 (2011).
[3]C. Ataca and S. Ciraci, J. Phys. Chem. C **115**, 13303 (2011).
[4]C. Ataca, H. Sahin, and S. Ciraci, J. Phys. Chem. C **116**, 8983 (2012).
[5]H.-P. Komsa, J. Kotakoski, S. Kurasch, O. Lehtinen, U. Kaiser, and A. V. Krasheninnikov, Phys. Rev. Lett. **109**, 035503 (2012).
[6]M. Chhowalla, H. S. Shin, G. Eda, L.-J. Li, K. P. Loh, and H. Zhang, Nat. Chem. **5**, 263 (2013).
[7]S. Horzum, H. Sahin, S. Cahangirov, P. Cudazzo, A. Rubio, T. Serin, and F. M. Peeters, Phys. Rev. B **87**, 125415 (2013).
[8]H. Sahin, S. Tongay, S. Horzum, W. Fan, J. Zhou, J. Li, J. Wu, and F. M. Peeters, Phys. Rev. B **87**, 165409 (2013).

[9]L. F. Mattheiss, Phys. Rev. B **8**, 3719 (1973).
[10]A. M. Gabovich, A. I. Voitenko, and M. Ausloos, Phys. Rep. **367**, 583 (2002).
[11]E. Morosan, H. W. Zandbergen, B. S. Dennis, J. W. G. Bos, Y. Onose, T. Klimczuk, A. P. Ramirez, N. P. Ong, and R. J. Cava, Nat. Phys. **2**, 544 (2006).
[12]S. A. Kivelson, E. Fradkin, and V. J. Emery, Nature (London) **393**, 550 (1998).
[13]S. Sachdev and S. C. Zhang, Science **295**, 452 (2002).
[14]K. Takada, H. Sakurai, E. J. Takayama-Muromachi, F. Izumi, R. A. Dilanian, and T. Sasaki, Nature (London) **422**, 53 (2003).
[15]J. A. Wilson, F. J. DiSalvo, and S. Mahasan, Adv. Rhys. **24**, 117 (1975).
[16]P. Fazekas and E. Tosatti, Philos. Mag. B **39**, 229 (1979).
[17]P. Fazekas and E. Tosatti, Physica B+C **99**, 183 (1980).
[18]C. B. Scruby, P. M. Williams, and G. S. Parry, Philos. Mag. **31**, 255 (1975).
[19]M. H. Whangbo and E. Canadell, J. Am. Chem. Soc. **114**, 9587 (1992).
[20]N. V. Smith, S. D. Kevan, and F. J. DiSalvo, J. Phys. C **18**, 3175 (1985).
[21]K. Rossnagel and N. V. Smith, Phys. Rev. B **73**, 073106 (2006).
[22]A. Spijkerman, J. L. de Boer, A. Meetsma, G. A. Wiegers, and S. van Smaalen, Phys. Rev. B **56**, 13757 (1997).
[23]A. M. Woolley and G. Wexler, J. Phys. C: Solid State Phys. **10**, 2601 (1977).
[24]M. H. Whangbo, J. Ren, E. Canadell, D. Louder, B. A. Parkinson, H. Bengel, and S. N. Magonov, J. Am. Chem. Soc. **115**, 3760 (1993).
[25]H. J. Crawack and C. Pettenkofer, Solid State Commun. **118**, 325 (2001).
[26]B. Sipos, A. F. Kusmartseva, A. Akrap, H. Berger, L. Forro, and E. Tutis, Nature Mater. **7**, 960 (2008).
[27]P. Xu, J. O. Piatek, P. H. Lin, B. Sipos, H. Berger, L. Forro, H. M. Ronnow, and M. Grioni, Phys. Rev. B **81**, 172503 (2010).
[28]L. J. Li, W. J. Lu, X. D. Zhu, L. S. Ling, Z. Qu, and Y. P. Sun, Europhys. Lett. **97**, 67005 (2012).
[29]R. Ang, Y. Tanaka, E. Ieki, K. Nakayama, T. Sato, L. J. Li, W. J. Lu, Y. P. Sun, and T. Takahashi, Phys. Rev. Lett. **109**, 176403 (2012).
[30]X. L. Wu and C. M. Lieber, Phys. Rev. Lett. **64**, 1150 (1990).
[31]R. C. Barrett, J. Nogami, and C. F. Quate, Appl. Phys. Lett. **57**, 992 (1990).